Science Advances
AAAS

advances.sciencemag.org/cgi/content/full/4/10/eaau6261/DC1

Supplementary Materials for

Atomic-level structure engineering of metal oxides for high-rate oxygen intercalation pseudocapacitance

Tao Ling, Pengfei Da, Xueli Zheng, Binghui Ge, Zhenpeng Hu, Mengying Wu, Xi-Wen Du, Wen-Bin Hu, Mietek Jaroniec, Shi-Zhang Qiao*

*Corresponding author. Email: s.qiao@adelaide.edu.au

Published 19 October 2018, *Sci. Adv.* **4**, eaau6261 (2018)
DOI: 10.1126/sciadv.aau6261

This PDF file includes:

Supplementary Figures

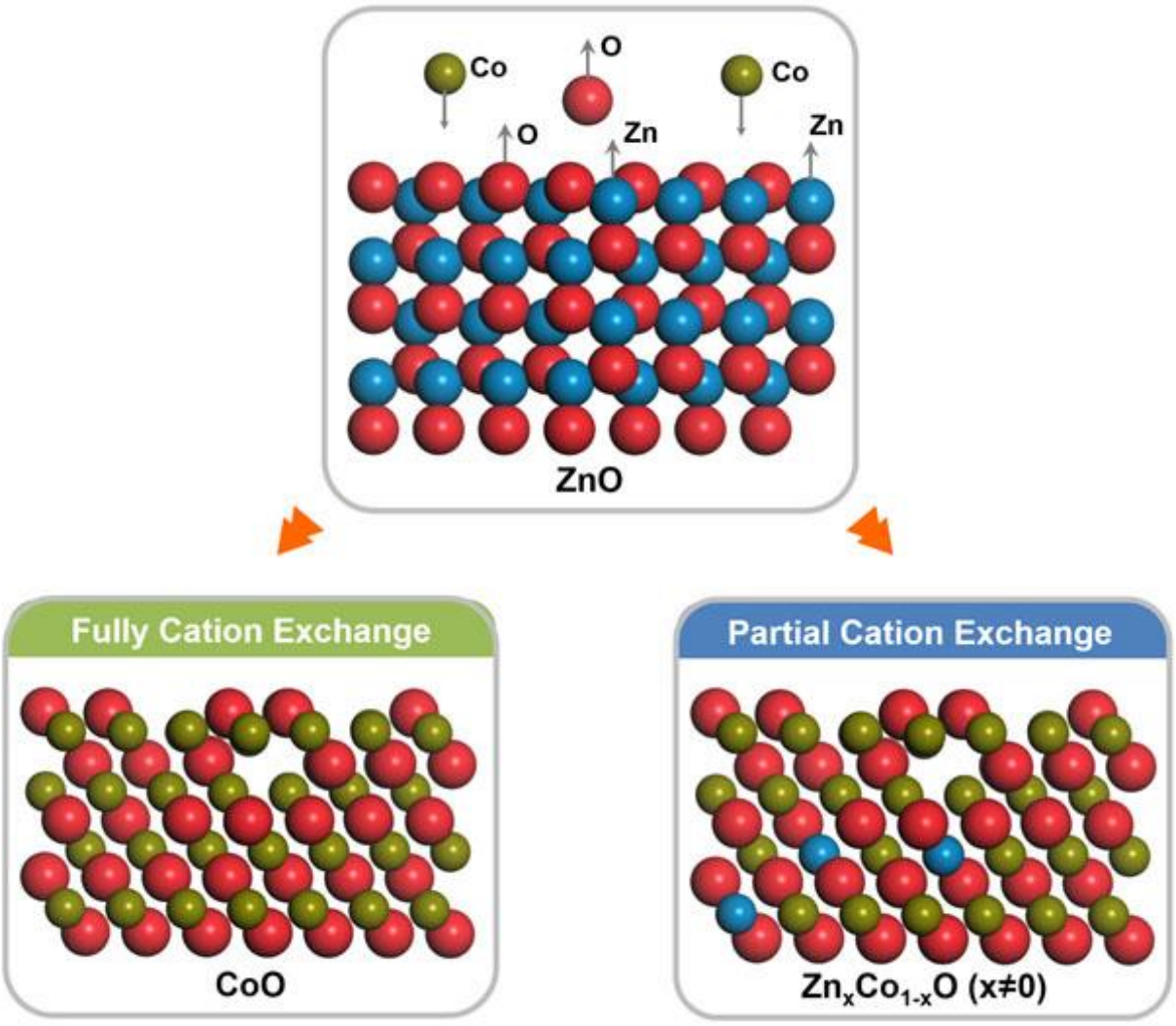

Fig. S1. Schematic diagram of the cation exchange methodology for the synthesis of $Zn_xCo_{1-x}O$ NRs. A complete replacement reaction of Zn^{2+} by Co^{2+} results in CoO NRs, while a partial replacement reaction of Zn^{2+} by Co^{2+} gives $Zn_xCo_{1-x}O$ ($x \neq 0$) NRs.

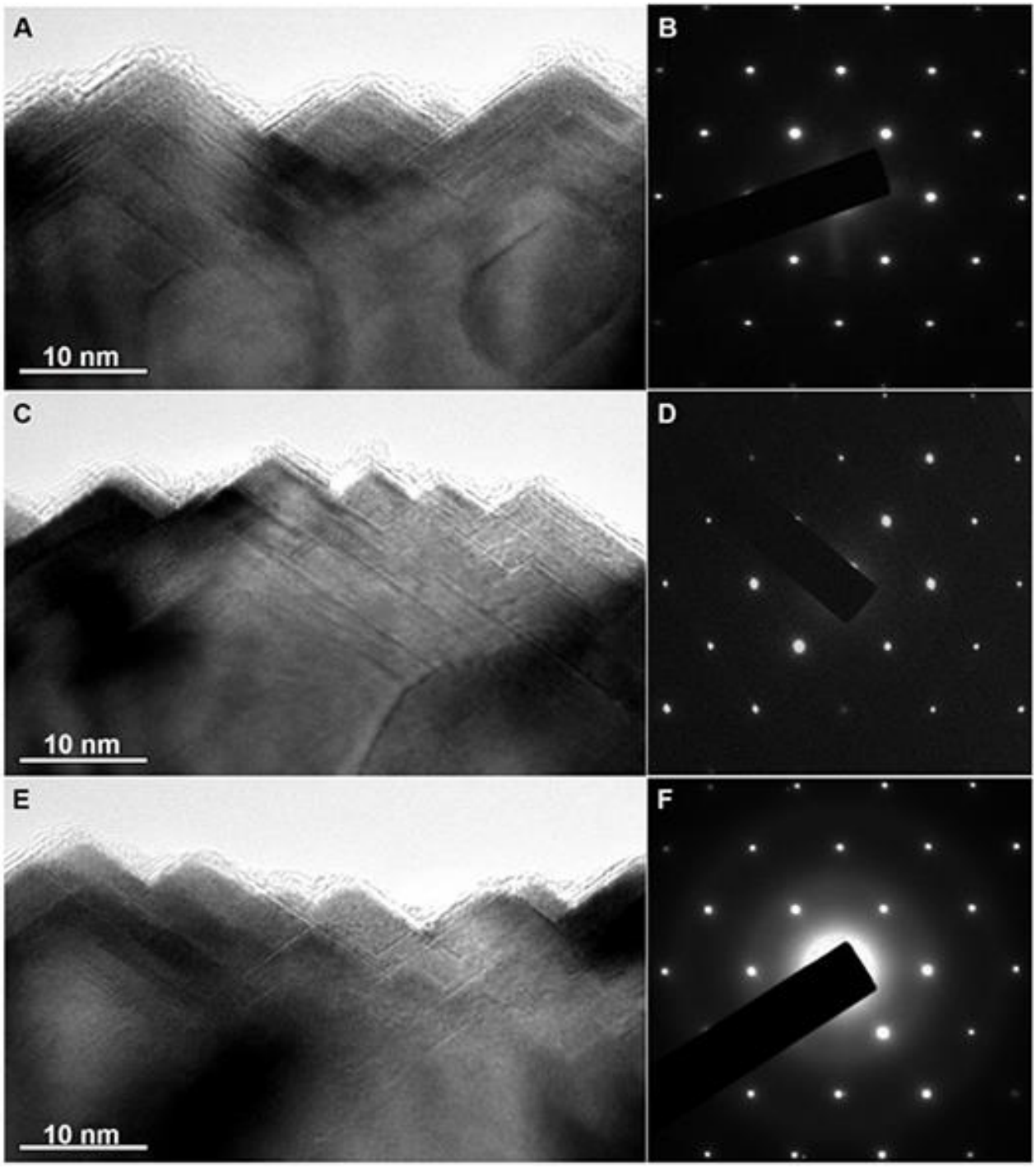

Fig. S2. TEM characterizations of $Zn_xCo_{1-x}O$ NRs. A, **C** and **E**, HRTEM image of a single NR of CoO, $Zn_{0.04}Co_{0.96}O$, and $Zn_{0.06}Co_{0.94}O$, respectively. **B**, **D** and **F**, Selected-area-electron-diffraction (SAED) patterns of CoO, $Zn_{0.04}Co_{0.96}O$, and $Zn_{0.06}Co_{0.94}O$ NR, respectively.

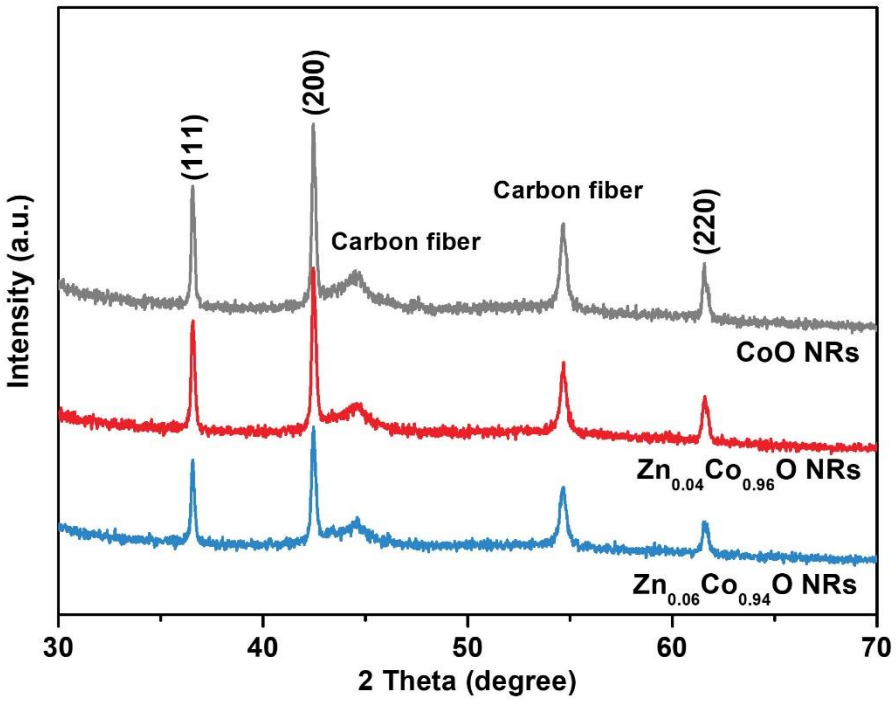

Fig. S3. X-ray diffraction (XRD) spectra of $Zn_xCo_{1-x}O$ NRs. The peaks are assigned to (111), (200) and (220) planes of the face-centered cubic (FCC) phase of CoO, and there are no visible defects, the second phase, or precipitation in the as-exchanged $Zn_xCo_{1-x}O$ NRs.

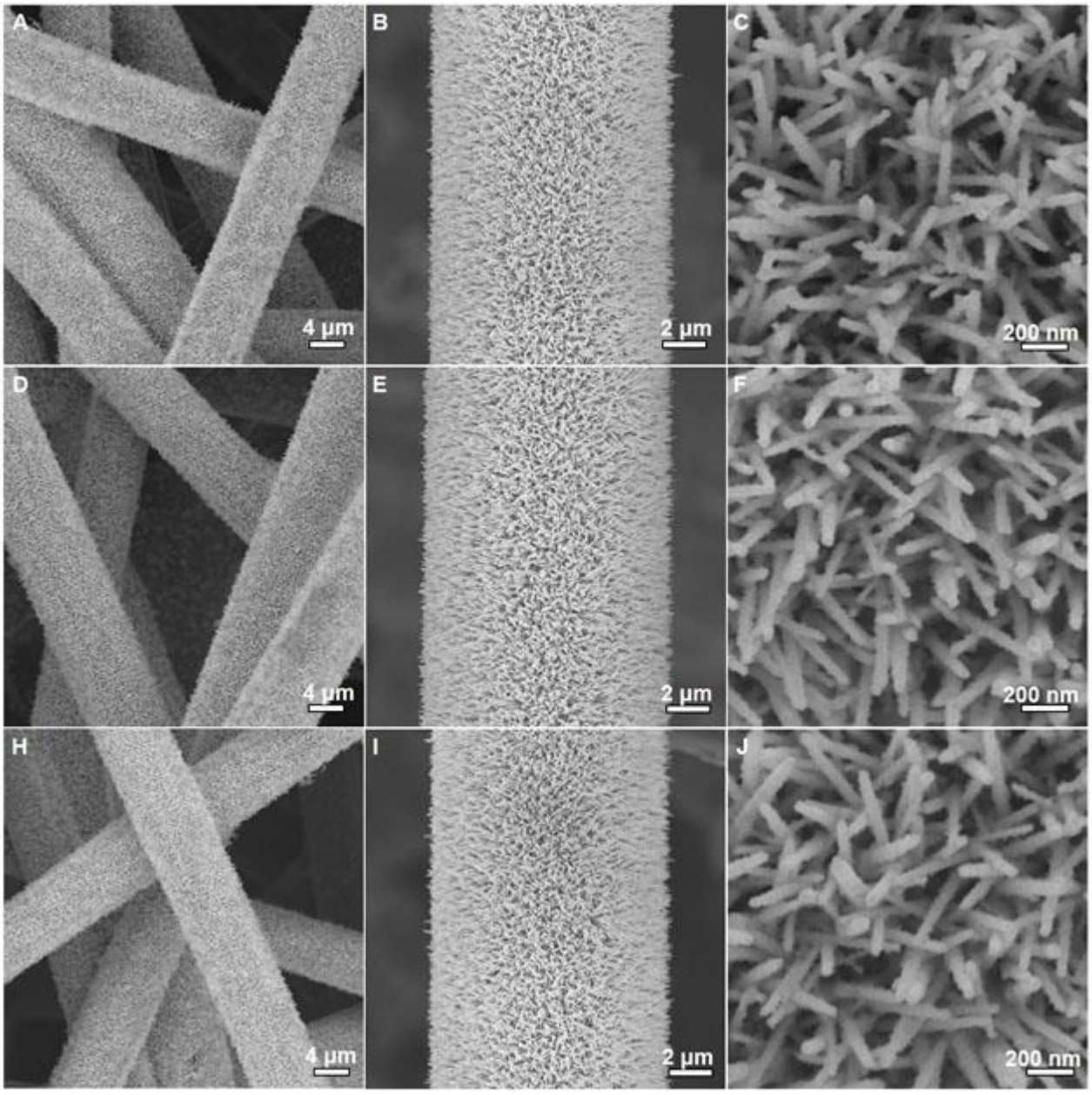

Fig. S4. SEM images of $Zn_xCo_{1-x}O$ NRs. A-C, CoO NRs. **D-F**, $Zn_{0.04}Co_{0.96}O$ NRs. **H-J**, $Zn_{0.06}Co_{0.94}O$ NRs.

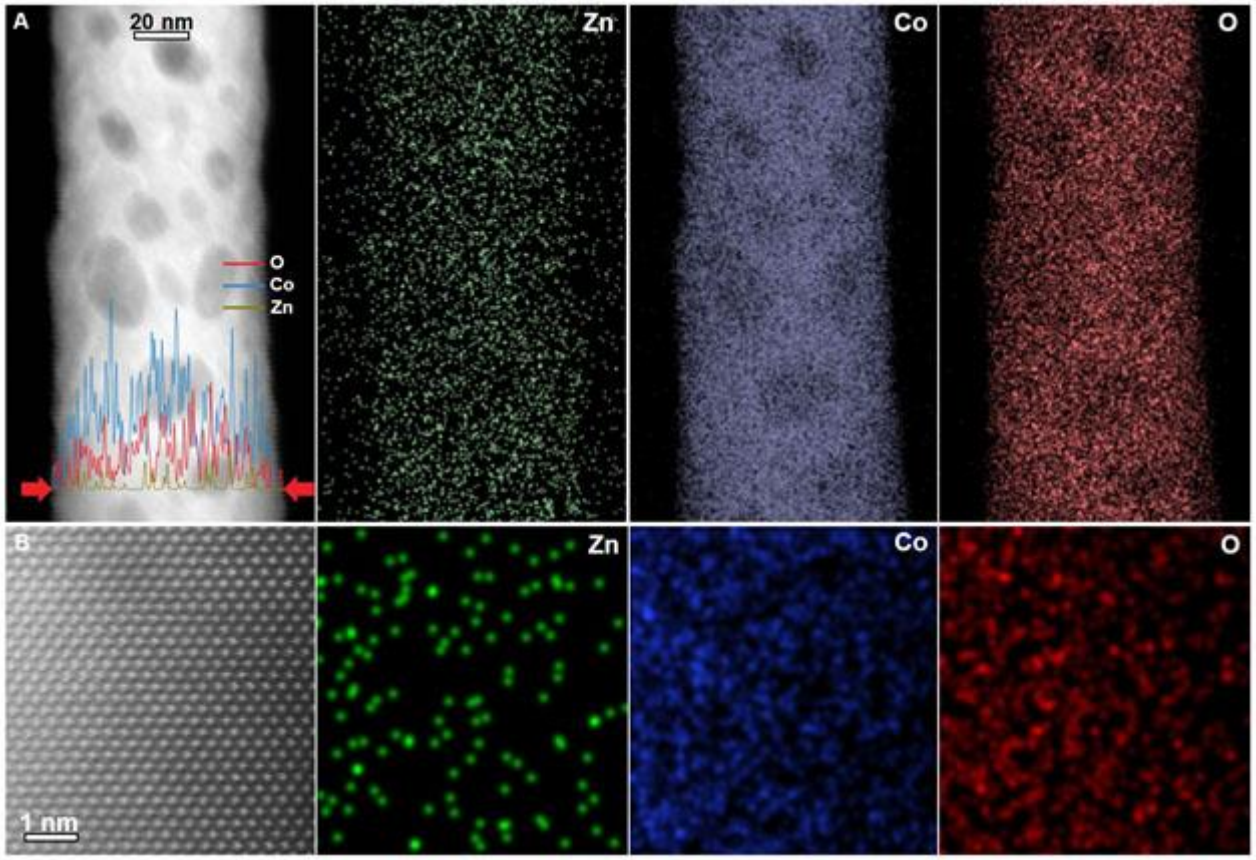

Fig. S5. Composition analysis of a single $Zn_{0.04}Co_{0.96}O$ NR. A, HAADF-STEM image and EDS elemental mapping of Zn, Co, and O elements in a single nanorod. In **A**, the linear scanning result shows that O, Co and Zn elements are distributed uniformly across the entire nanorod. **B**, Sub-nm spatial resolution elemental mapping of Zn, Co, and O elements showing uniform distribution of Zn dopant on a single nanorod at the atomic level.

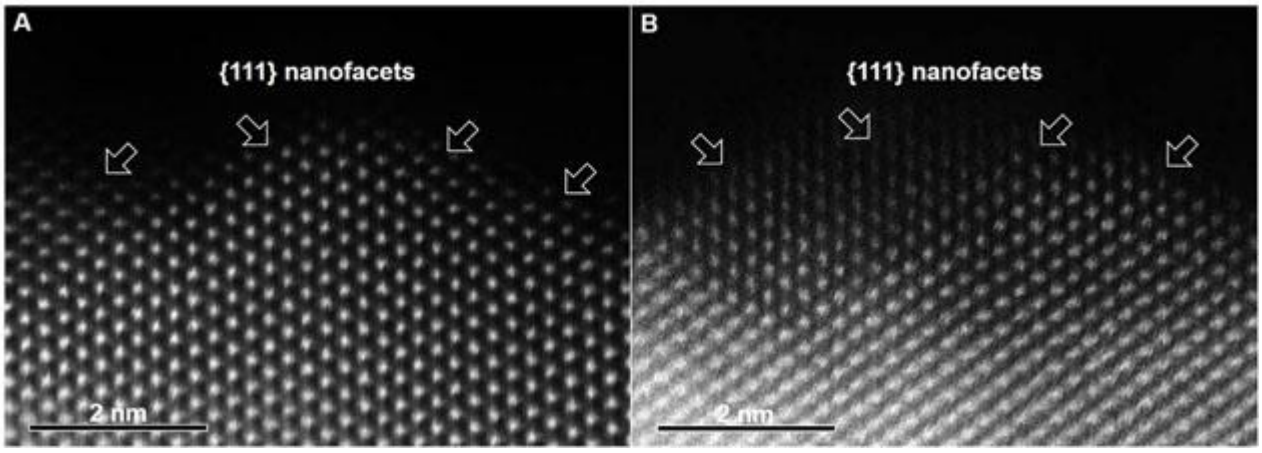

Fig. S6. HAADF-STEM characterization of the as-exchanged $Zn_xCo_{1-x}O$ NRs. A, CoO NR. **B**, $Zn_{0.06}Co_{0.94}O$ NR.

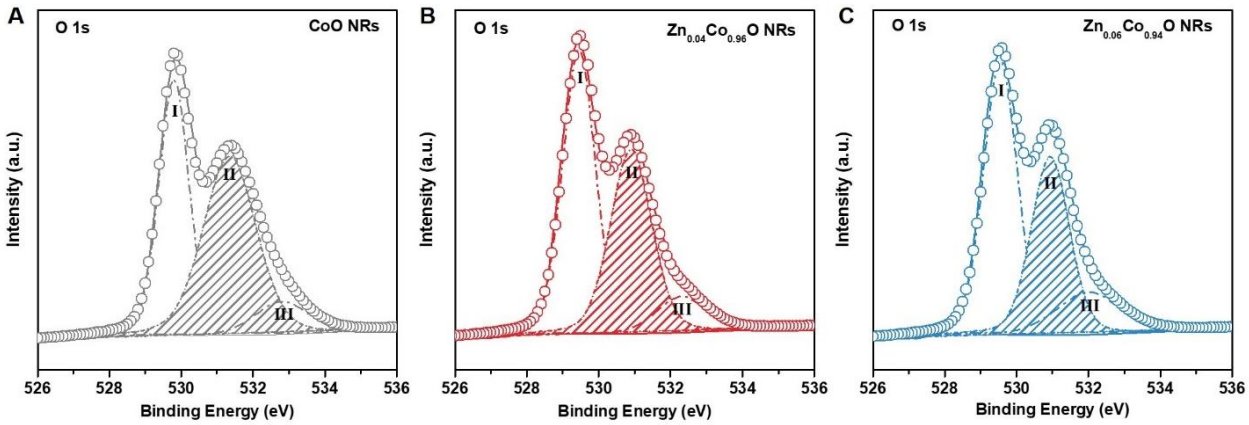

Fig. S7. X-ray photoelectron spectroscopy O 1s spectra of $Zn_xCo_{1-x}O$ NRs. A, CoO. **B**, $Zn_{0.04}Co_{0.96}O$. **C**, $Zn_{0.06}Co_{0.94}O$. The circles and lines are experimental and deconvolution data, respectively. In **A-C**, the peak with low binding energy (Peak I) is assigned to the lattice oxygen (O_L) (*Analyt. Chem.* 1975, 47, 2208-2213), whereas peak II with middle binding energy is attributed to a high number of defect sites with lower oxygen coordination (*J. Electron Spect. Rel. Phen.* 1995, 71, 61-71; *Angew. Chem. Int. Ed.* 2015, 54, 7399-7404), and peak III with high binding energy is associated with surface-adsorbed water molecules (*Angew. Chem. Int. Ed.* 2015, 54, 7399-7404). Evidently, a significant amount of O-vacancies is present on the as-exchanged NRs, and the total quantity of O-vacancies increases in the following order $Zn_{0.06}Co_{0.94}O$ NRs < $Zn_{0.04}Co_{0.96}O$ NRs < CoO NRs.

The formation of large quantities of O-vacancies on the surface of $Zn_xCo_{1-x}O$ NRs arises from the ion exchange process, during which O-vacancies control the communication between the parent ZnO and product $Zn_xCo_{1-x}O$ NRs (*Chem. Soc. Rev.* 2013, 42, 89-96). Moreover, our previous DFT calculations reveal that the energy of O-vacancies formation on {111} facets is significantly lower than that on {100} and {110} facets (*Nat. Commun.* 2016, 7, 12876). This explains why large amounts of O-vacancies are present on {111} nanofacets of $Zn_xCo_{1-x}O$ NRs. Overall, the cation exchange drives the formation of {111} nanofacets on the surface of $Zn_xCo_{1-x}O$ NRs, thus facilitates the creation of O-vacancies, which in turn accelerate the cation exchange process. It should be noted that although engineering of facets (*Science* 2015, 349, 412–416; *Science* 2007, 316, 732–735) or defects (*Nat. Mater.* 2016, 15, 48–53; *Angew. Chem. Int. Ed.* 2013, 52, 2474–2477) have been investigated for many materials, the formation of defects on the desired facets and understanding their role in the capacitive reactions at the atomic level are still lacking.

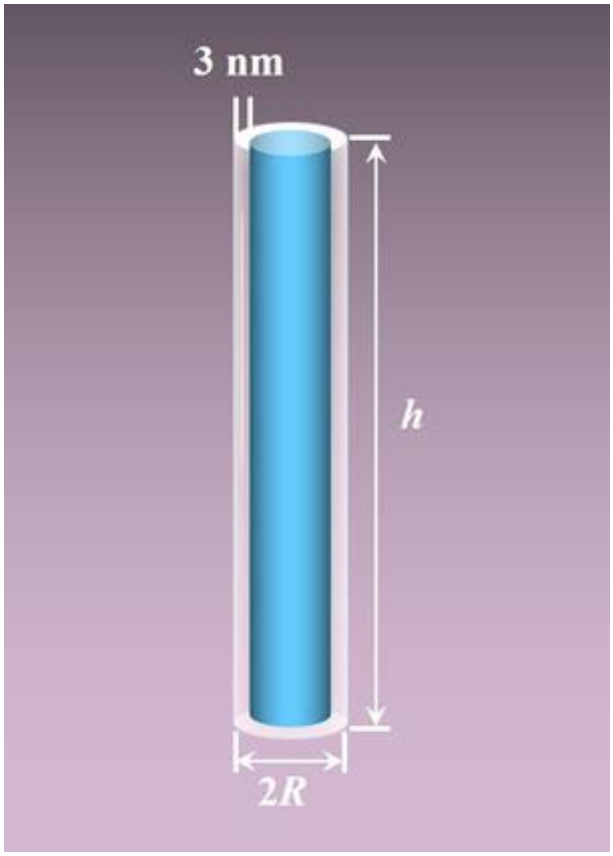

Fig. S8. Schematic illustration of the spatial distribution of O vacancies in a single $Zn_xCo_{1-x}O$ NR.

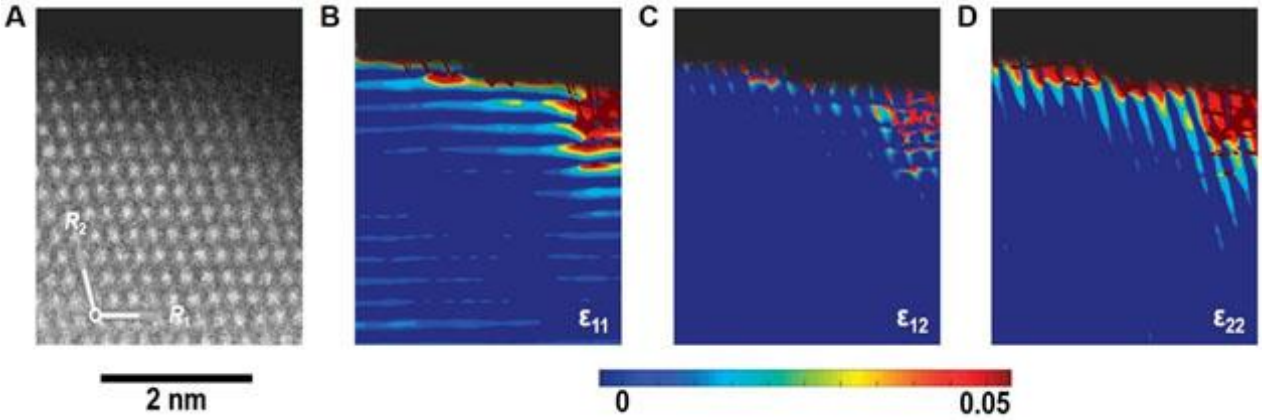

Fig. S9. Analysis of lattice expansion of the surface region of $Zn_xCo_{1-x}O$ NRs. A, Atomic resolution HAADF-STEM image of a typical {111} nanofacet exposed on the surface of $Zn_xCo_{1-x}O$, indicating the lattice vectors $\boldsymbol{R_1}$ and $\boldsymbol{R_2}$ used as a reference for the strain analysis. **B**-**D**, Contour plots of the strain component ε_{11} (**B**), ε_{12} (**C**) and ε_{22} (**D**) relative to the reference values.

Geometric phase analysis (GPA) (*Ultramicroscopy* 1998, 74, 131-146) was used to obtain the strain tensor maps of the surface of an individual $Zn_xCo_{1-x}O$ NRs. The derivation of the displacement field gives the strain field

$$\varepsilon_{11} = \partial u_1(R) / \partial R_1 \quad (1)$$

$$\varepsilon_{22} = \partial u_2(R) / \partial R_2 \quad (2)$$

$$\varepsilon_{12} = 1/2(\partial u_1(R) / \partial R_2 + \partial u_2(R) / \partial R_1) \quad (3)$$

where R is a position in **A**, $u(R)$ is the vectorial representation of the displacement field. GPA generates strain maps **(B-D**) with color contours directly illustrating the location of the lattice strain, suggesting 3~5% lattice expansion on the surface of $Zn_xCo_{1-x}O$ NRs.

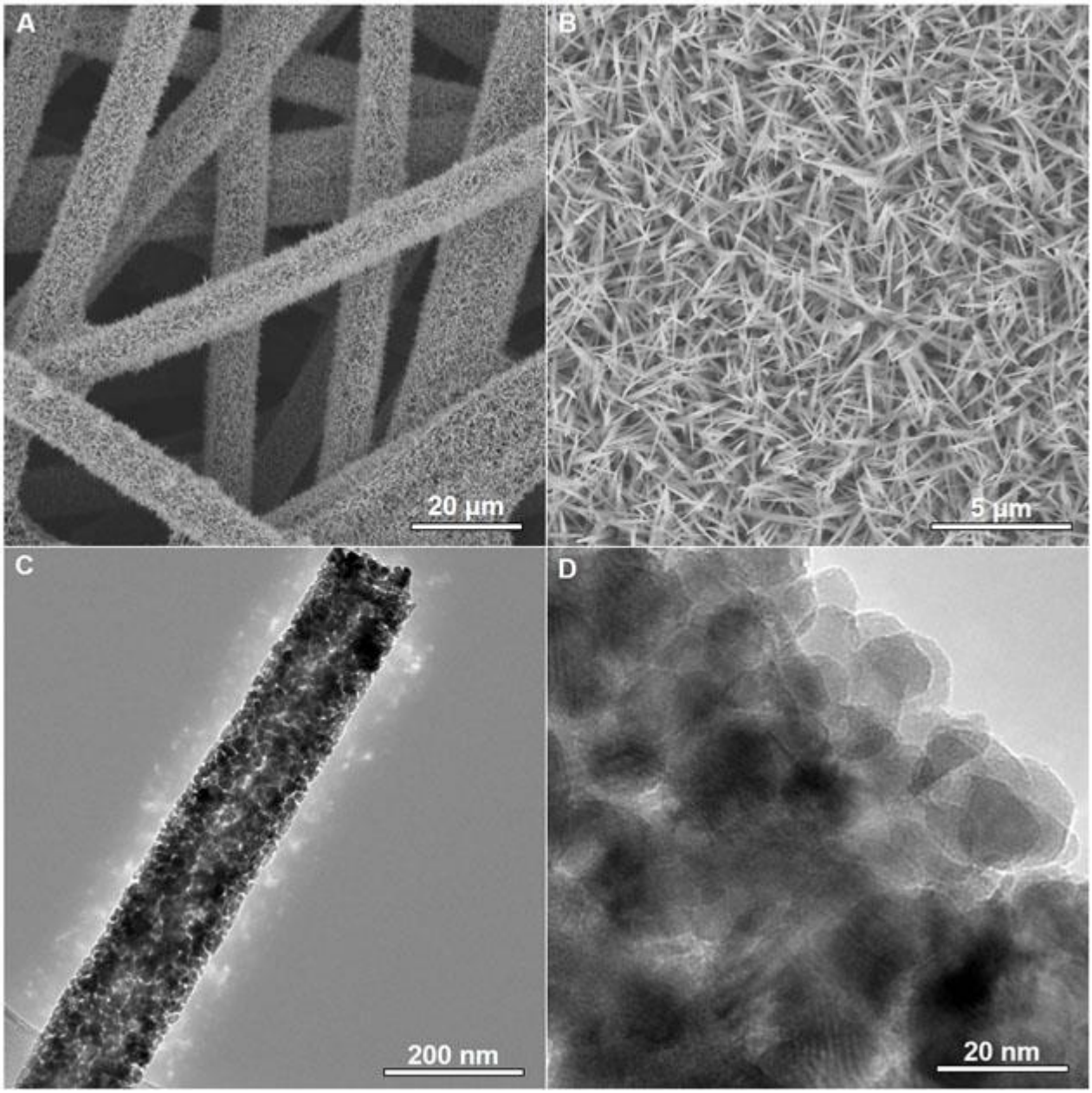

Fig. S10. Characterization of P-$Zn_xCo_{1-x}O$ NRs fabricated directly on CFP. A and **B**, Low and high magnification SEM image, respectively. **C** and **D**, Low and high magnification TEM image of an individual P-$Zn_xCo_{1-x}O$ NR, respectively.

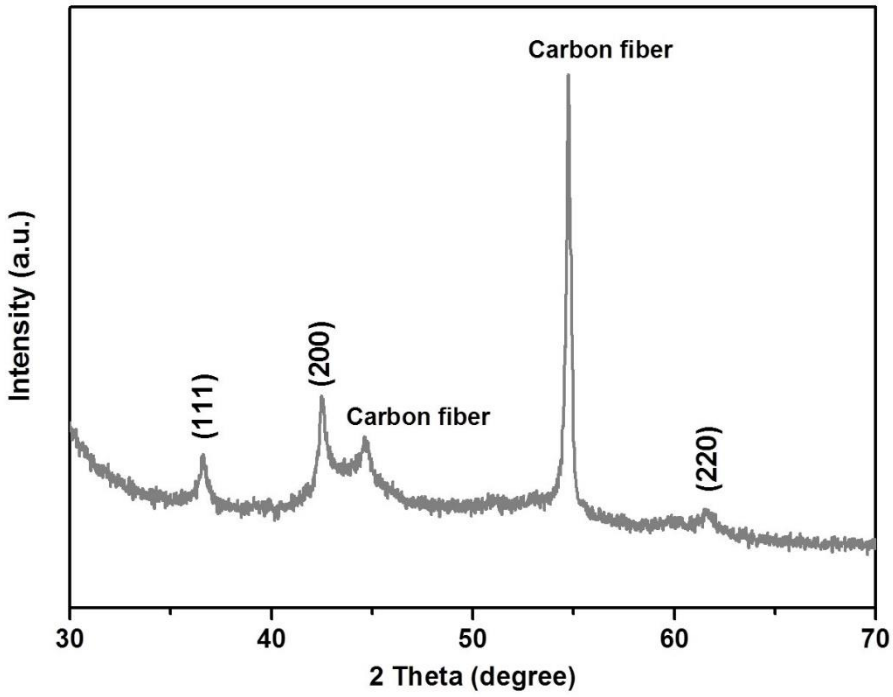

Fig. S11. XRD spectrum of P-$Zn_xCo_{1-x}O$ NRs fabricated on CFP. The peaks are attributed to (111), (200) and (220) planes of the FCC phase of CoO.

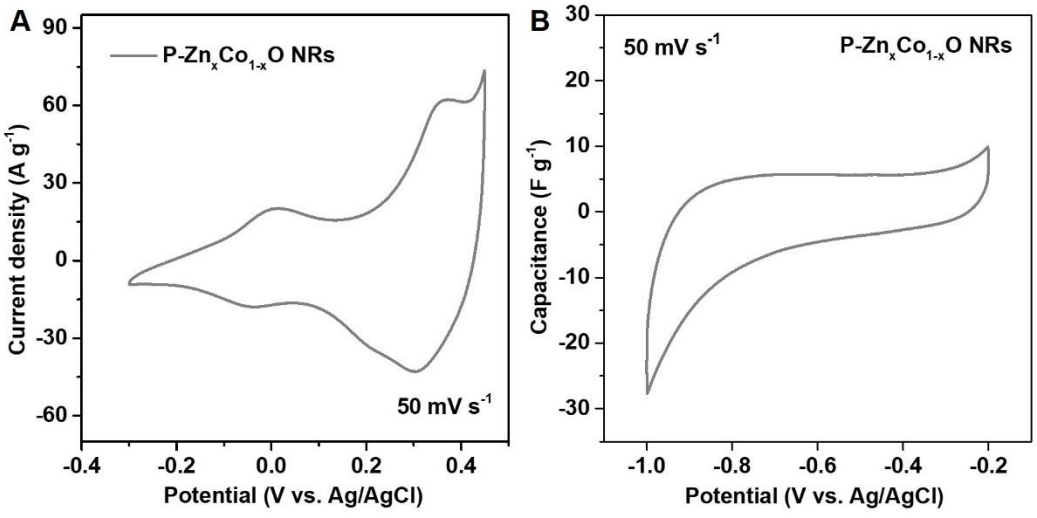

Fig. S12. CV curves of P-$Zn_xCo_{1-x}O$ NRs at potential window of (A) -0.4 ~ 0.4 $V_{Ag/AgCl}$, (B) -1.0 ~ -0.2 $V_{Ag/AgCl}$.

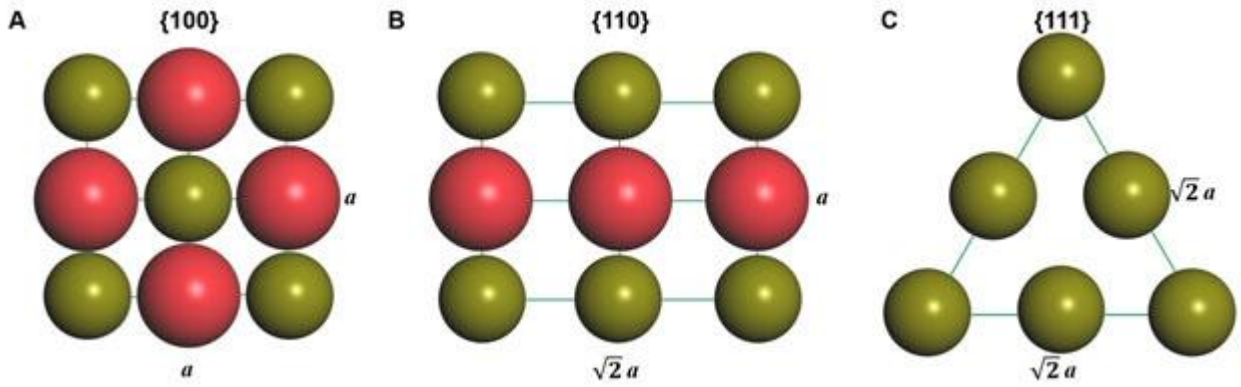

Fig. S13. Atom arrangements on low index planes of CoO. A, {100}. **B**, {110}. **C**, {111}-Co. Colour codes: bluish yellow and red spheres denote cobalt and oxygen atoms, respectively.

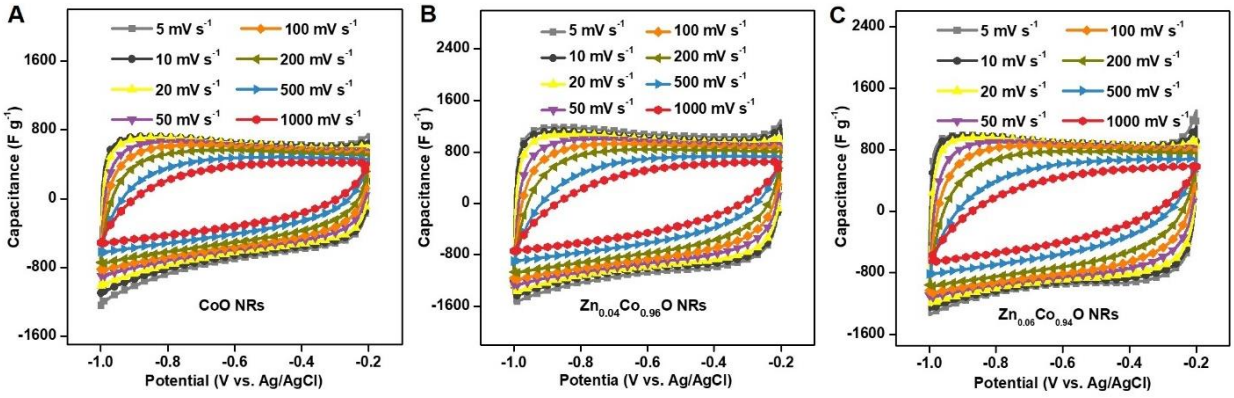

Fig. S14. CV curves of $Zn_xCo_{1-x}O$ NRs collected at scan rates from 5 to 1000 mV s^{-1}. A, CoO NRs. **B**, $Zn_{0.04}Co_{0.96}O$ NRs. **C**, $Zn_{0.06}Co_{0.94}O$ NRs.

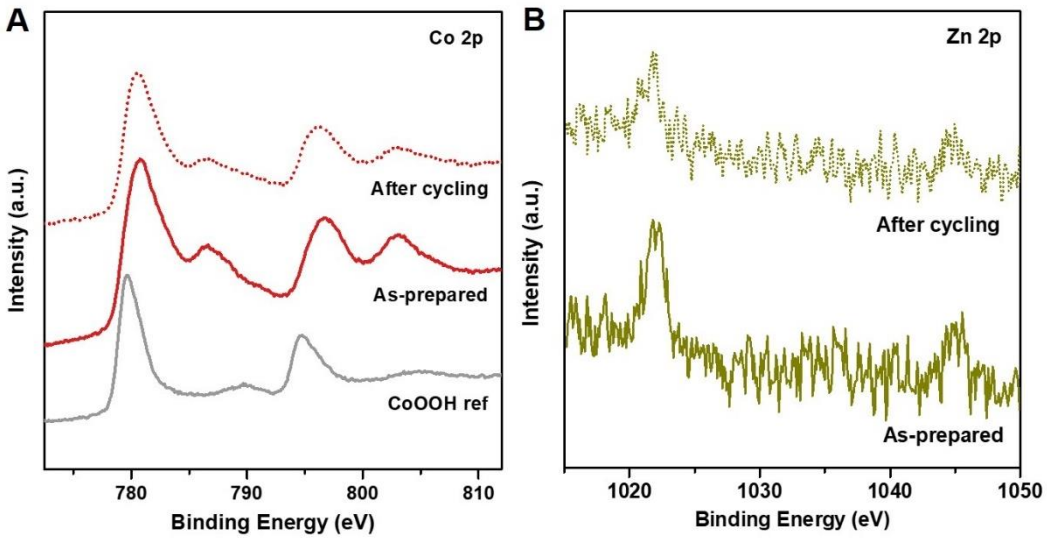

Fig. S15. XPS spectra of $Zn_{0.04}Co_{0.96}O$ NRs before and after the cycling test. A, Co 2p. **B**, Zn 2p.

In **A**, CoOOH is introduced as the reference. No noticeable peak shift was observed on the Co 2p XPS spectrum of $Zn_{0.04}Co_{0.96}O$ NRs after cycling test in comparison to that of the fresh sample, demonstrating the cobalt oxidation state remained at about 2. In addition, the inductively coupled plasma mass spectrometry (ICP-MS) measurements show that the doped Zn-ions are hardly solved into electrolyte during electrochemical cycling (table S2).

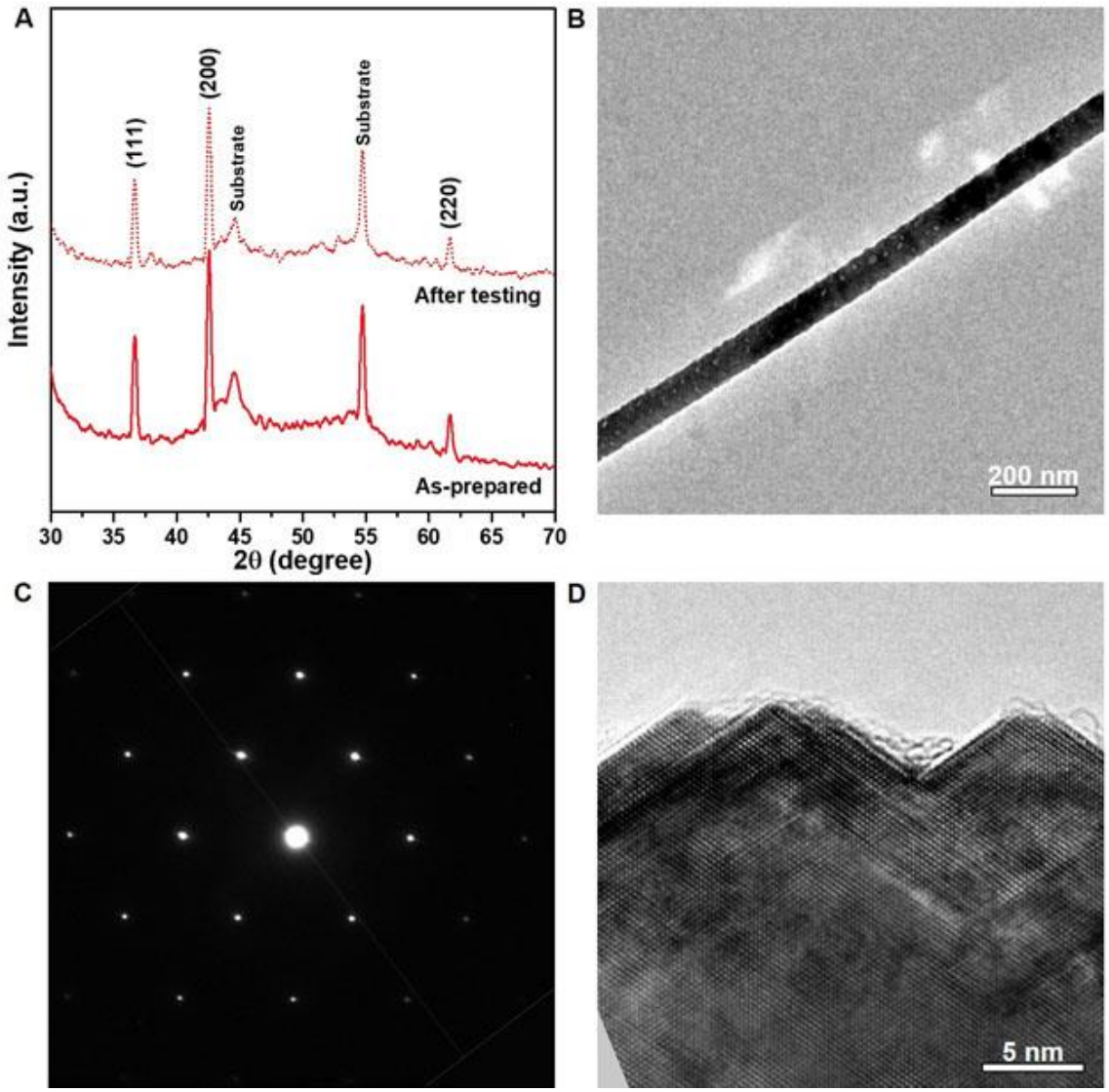

Fig. S16. Structural characterizations of $Zn_{0.04}Co_{0.96}O$ NRs after the cycling test. A, XRD. **B,** low-magnification TEM image. **C**, SAED pattern. **D**, HRTEM image.

The XRD pattern in **a** of $Zn_xCo_{1-x}O$ NRs after the electrochemical test shows no phase change in comparison to the fresh $Zn_xCo_{1-x}O$ NRs, which is further supported by the SAED characterization (**C**). Moreover, as displayed clearly in **D**, the {111} nanofacets on the outermost surface of $Zn_xCo_{1-x}O$ NRs are kept intact after testing. Based on these collective results, we demonstrate that the geometric structure of the as-synthesized $Zn_xCo_{1-x}O$ NRs are robust enough to withstand the lattice strain generated by the oxygen insertion/extraction processes, which should be mainly attributed to the large amount of O-vacancies and lattice expansion located on the surface and near-surface region of $Zn_xCo_{1-x}O$ NRs as well as their porous structure (Fig. 2B and fig. S21).

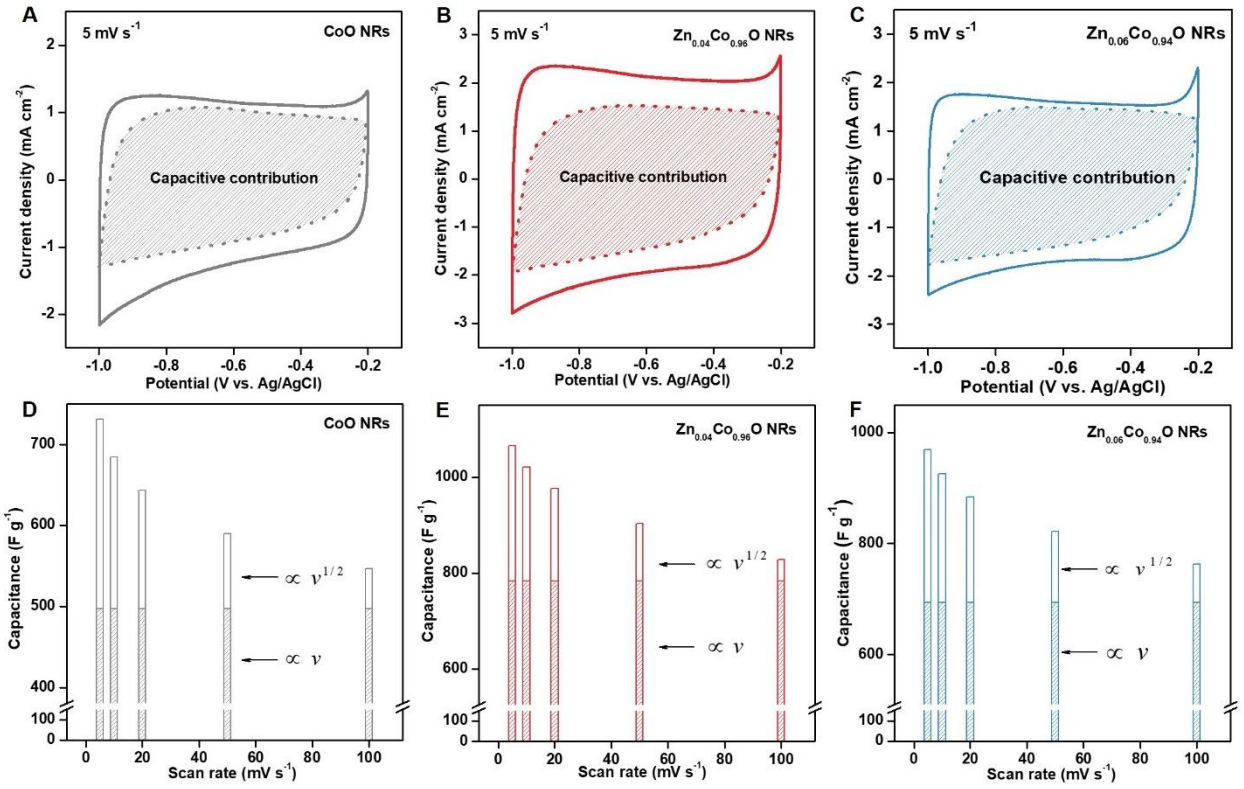

Fig. S17. Deconvolution of diffusion-controlled and capacitive-like capacitance in $Zn_xCo_{1-x}O$ NRs. A-C, CV curves at 5 mV s^{-1}. **D-F**, Deconvolution of charge contribution as a function of scan rates.

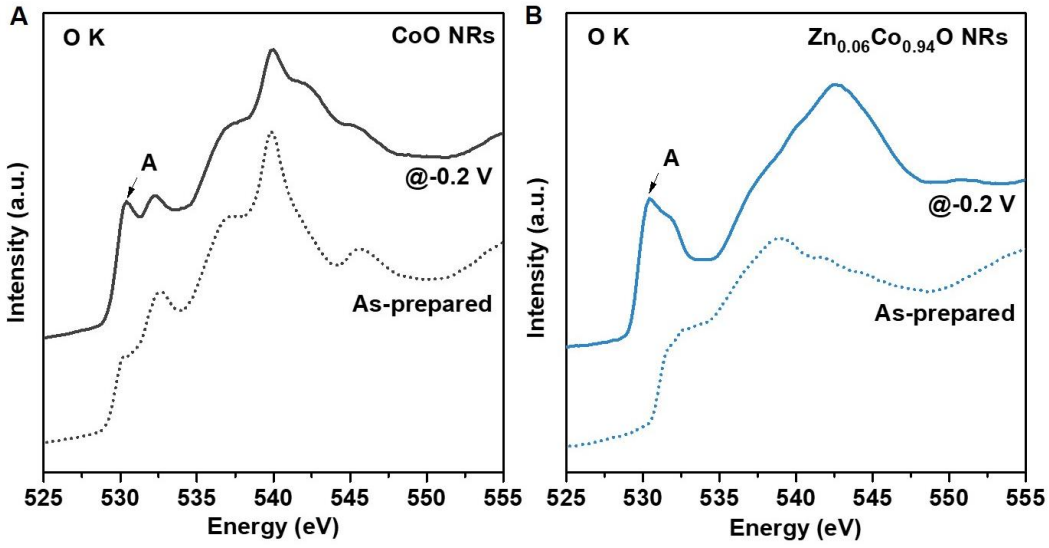

Fig. S18. O-K edge x-ray absorption near-edge structure spectra of $Zn_xCo_{1-x}O$ NRs before and processed at −0.2 $V_{Ag/AgCl}$. A, CoO NRs. **B**, $Zn_{0.06}Co_{0.94}O$ NRs.

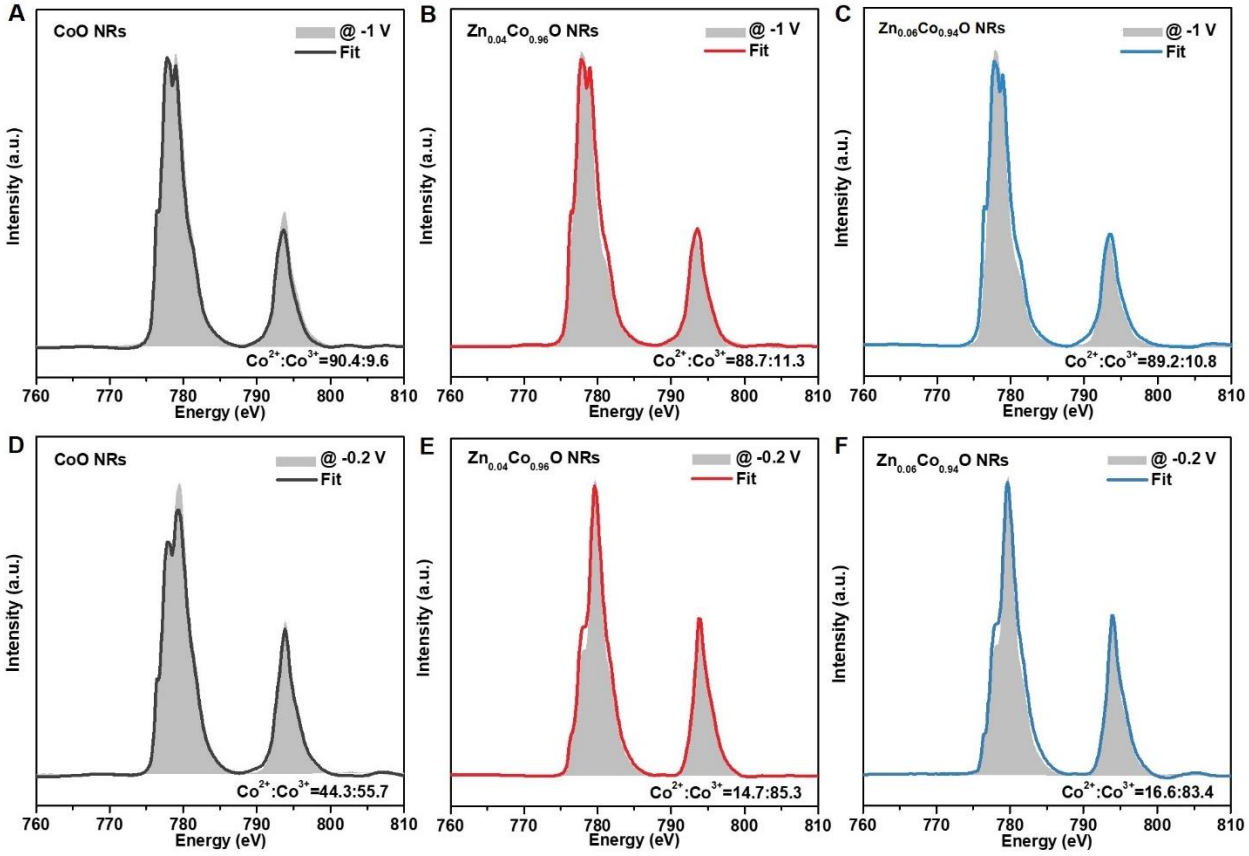

Fig. S19. Analysis of Co-$L_{2,3}$ edge XAS spectra of $Zn_xCo_{1-x}O$ NRs. Data were fitted using a linear combination of the spectra (*Science*, 2016, 352, 333-337) from references CoO (for Co^{2+}) and Co_2O_3 (for Co^{3+}). **A** and **D**, CoO NRs at -1 and -0.2 $V_{Ag/AgCl}$, respectively. **B** and **E**, $Zn_{0.04}Co_{0.96}O$ NRs at -1 and -0.2 $V_{Ag/AgCl}$, respectively. **C** and **F**, $Zn_{0.06}Co_{0.94}O$ NRs at -1 and -0.2 $V_{Ag/AgCl}$, respectively.

The average Co oxidation state change for CoO NRs, $Zn_{0.04}Co_{0.96}O$ NRs, and $Zn_{0.06}Co_{0.94}O$ NRs is about 0.46, 0.74, and 0.72, respectively (i.e., by 0.46, 0.74, and 0.72 $\bar{e}$ per Co atom, respectively). It is noteworthy that the small difference in the oxidation state of cobalt present in $Zn_{0.04}Co_{0.96}O$ and $Zn_{0.06}Co_{0.94}O$ NRs is due to the tiny difference in the O-vacancy concentrations (table S1).

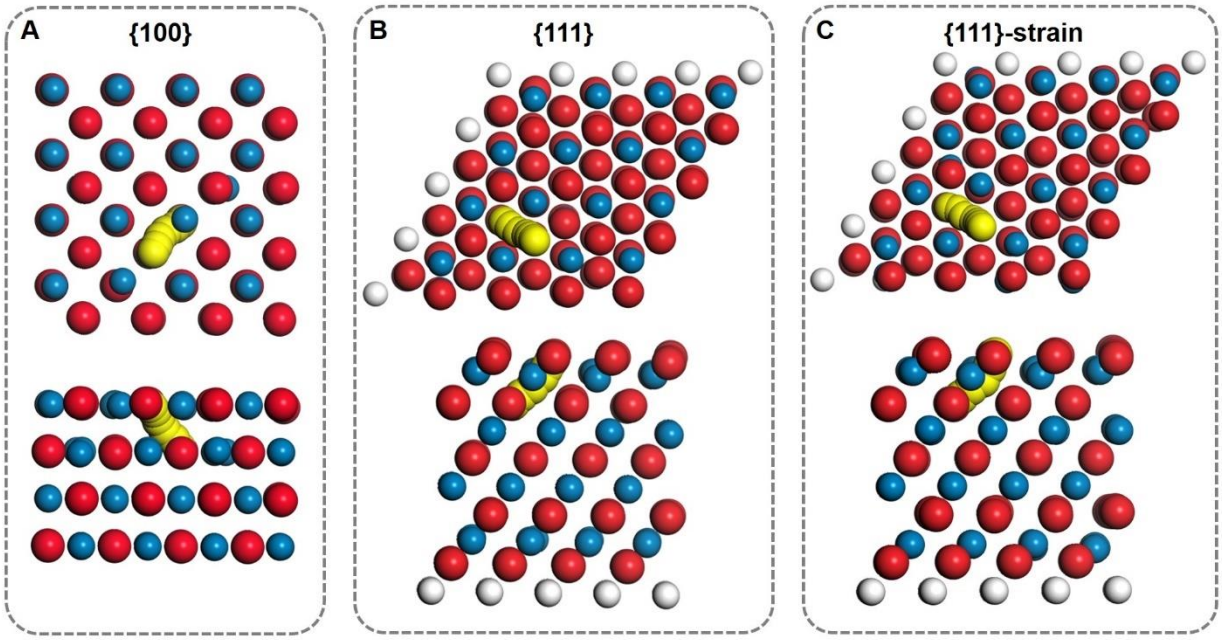

Fig. S20. Top-view and side-view illustration of O vacancy diffusion path through different surface facets. A, {100}. **B**, {111}. **C**, {111} with 3% lattice expansion. To model the O-vacancy diffusion through {100} surface, four Co-O layers (127 atoms) with a supercell size of a=b=12.07Å, c=21.80Å, α=β=γ=90º were employed. The {111} model consists of four Co layers, five O layers and one H layer (159 atoms) with a=b=12.07Å, c=29.78Å, α=β=90º, γ=120º. For the strained {111} structure, the lattice parameters of the unit cell were elongated by 3%. Colour codes: blue and red spheres denote respectively cobalt and oxygen atoms, and yellow and white spheres denote respective O-vacancy and hydrogen atoms.

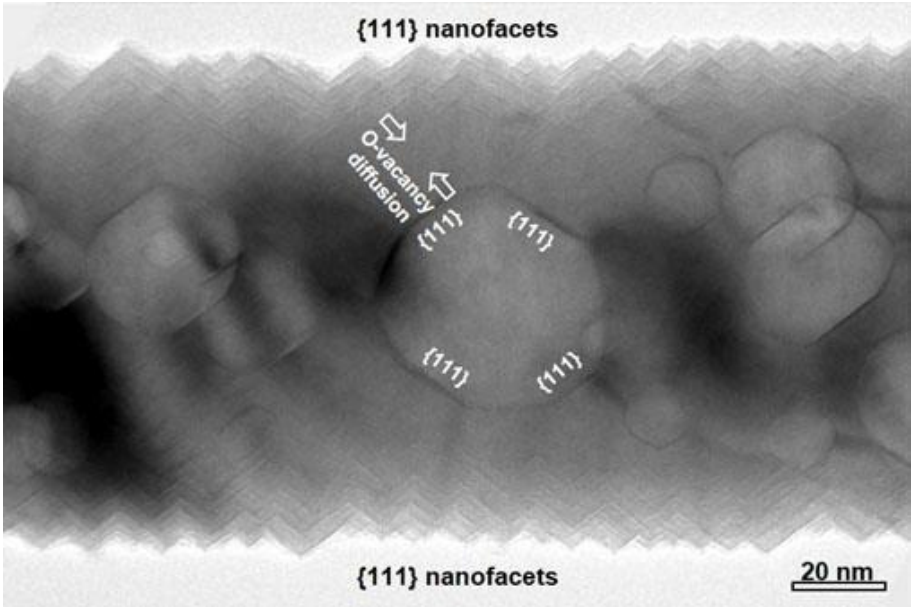

Fig. S21. TEM image of an individual $Zn_xCo_{1-x}O$ NR. As can be seen, numerous nanopores with well-defined {111} sidewalls are present inside $Zn_xCo_{1-x}O$ NRs.

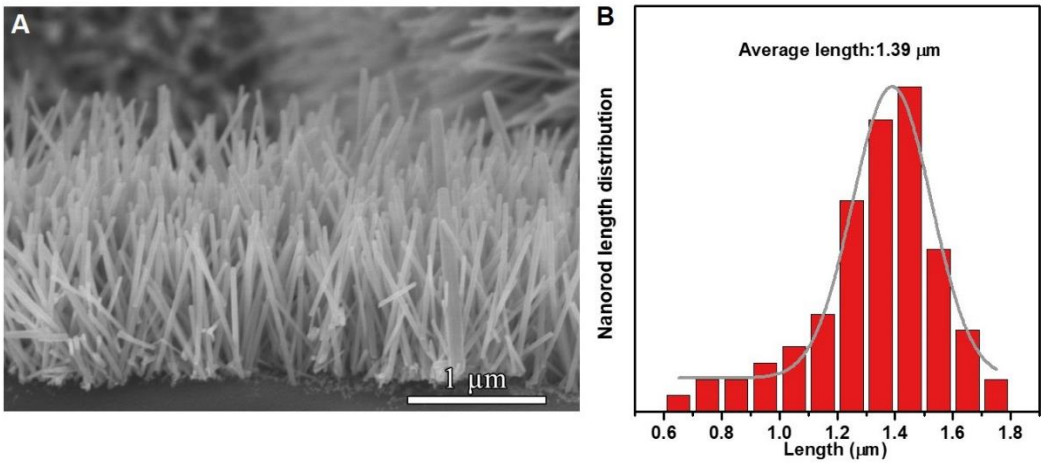

Fig. S22. Length distribution of $Zn_xCo_{1-x}O$ NRs fabricated directly on CFP. A, Cross-section SEM image. **B**, Length histogram of $Zn_xCo_{1-x}O$ NRs and corresponding Gaussian fit.

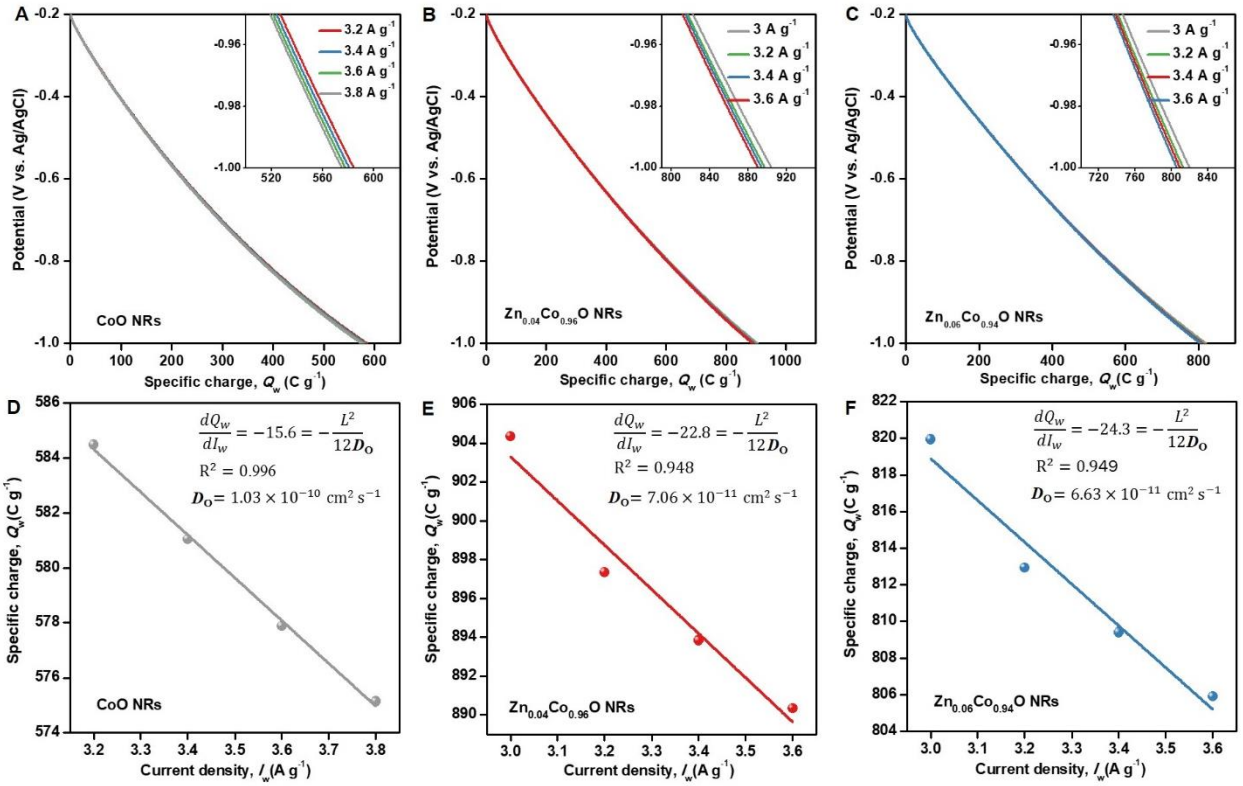

Fig. S23. Diffusion rate calculations for $Zn_xCo_{1-x}O$ NRs. A and **D**, CoO NRs. **B** and **E**, $Zn_{0.04}Co_{0.96}O$ NRs. **C** and **F**, $Zn_{0.06}Co_{0.94}O$ NRs.

The potential range shown in **A**, **B**, **C** is the corresponding potential window in galvanostatic charge-discharge plots. The chemical diffusion coefficient of oxygen (D_O) was calculated using the following equation (*Sci. Rep.* 2012, 2, 601)

$$\frac{dQ_w}{dI_w} = -\frac{L^2}{12D_O} \tag{4}$$

where L is the average length of $Zn_xCo_{1-x}O$ NRs obtained from fig. S22.

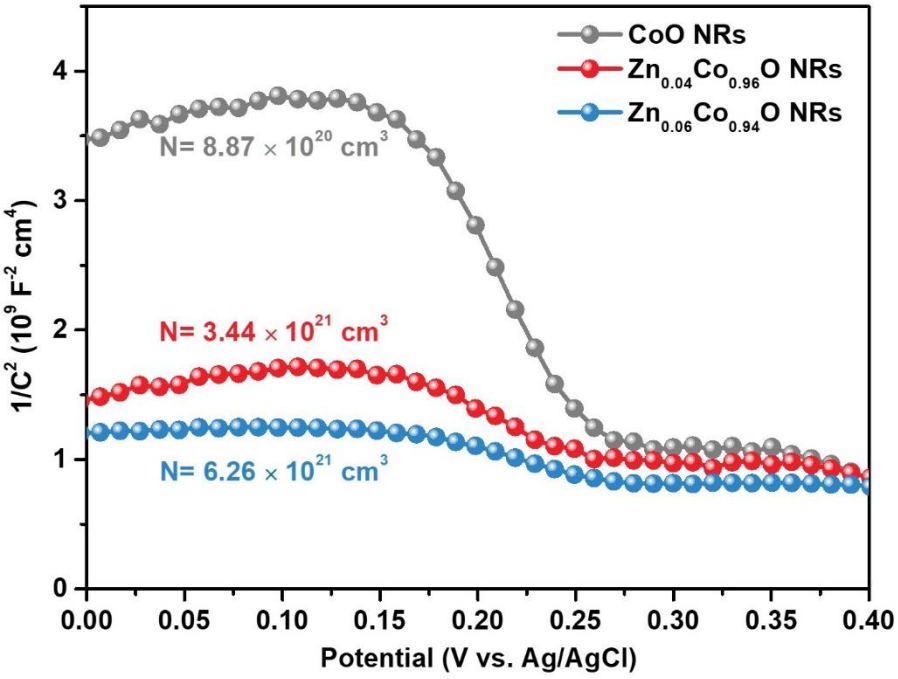

Fig. S24. M-S plots for $Zn_xCo_{1-x}O$ NRs. The hole density (*N*) can be calculated from the slopes of the M-S plots using the following equation (*Electroanal. Chem. Interfacial* 1975, 65, 163-175)

$$\frac{dC^{-2}}{dV} = \frac{-2}{q\varepsilon_0\varepsilon_r NA^2} \tag{5}$$

where *A* is the surface area of the sample studied, ε_r is the dielectric constant of CoO with the value of 5.4.

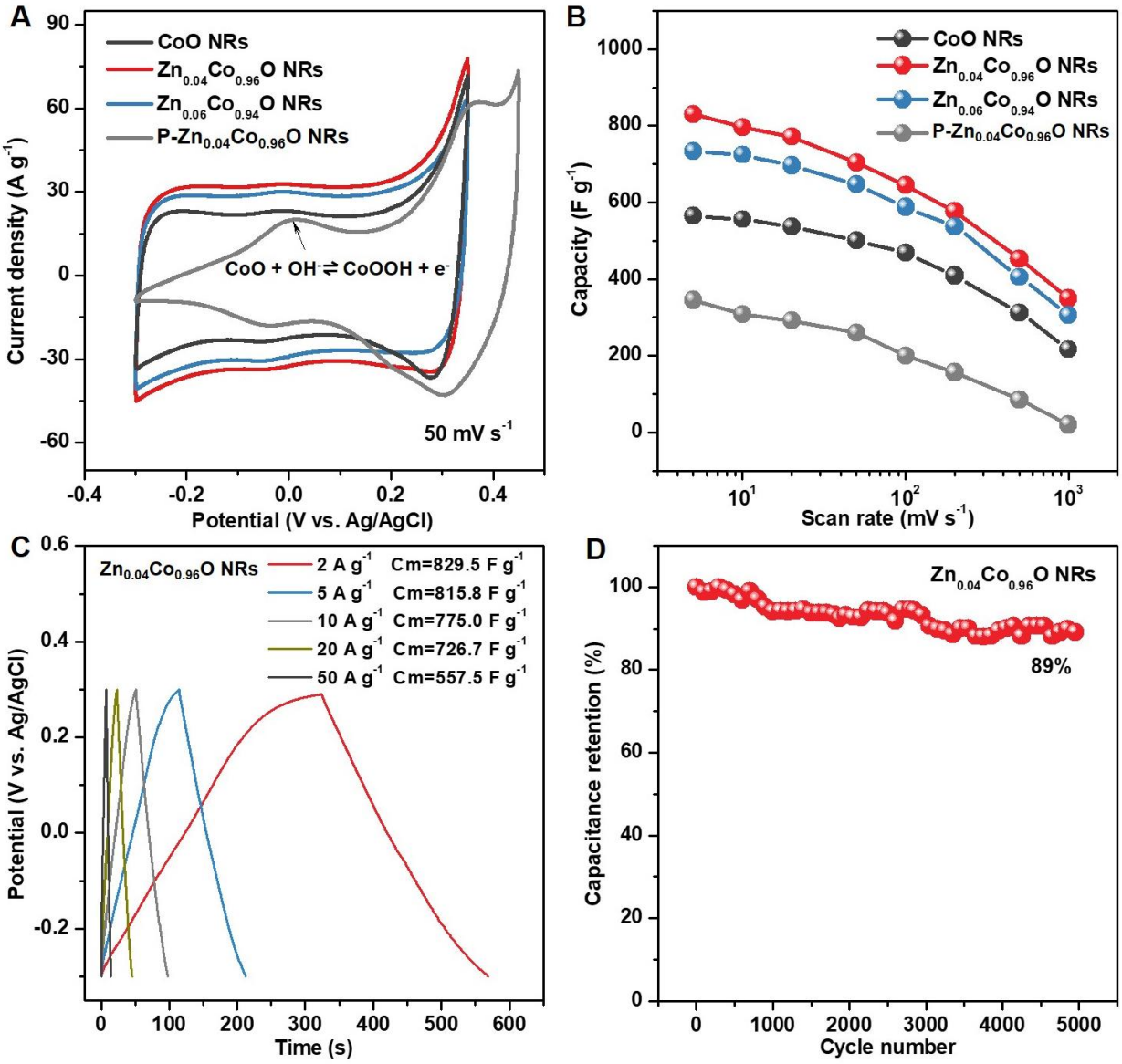

Fig. S25. Electrochemical performance of $Zn_xCo_{1-x}O$ NRs as compared with P-$Zn_xCo_{1-x}O$ NRs. A, CV curves at 50 mV s^{-1}. **B**, Specific capacity as a function of sweep rate between 5 and 1000 mV s^{-1}. **C**, Galvanostatic cycling profiles of $Zn_{0.04}Co_{0.96}O$ NRs collected at 2, 5, 10, 20, and 50 A g^{-1}. **D**, Capacitance retention of $Zn_{0.04}Co_{0.96}O$ NRs by galvanostatic cycling at 10 A g^{-1}.

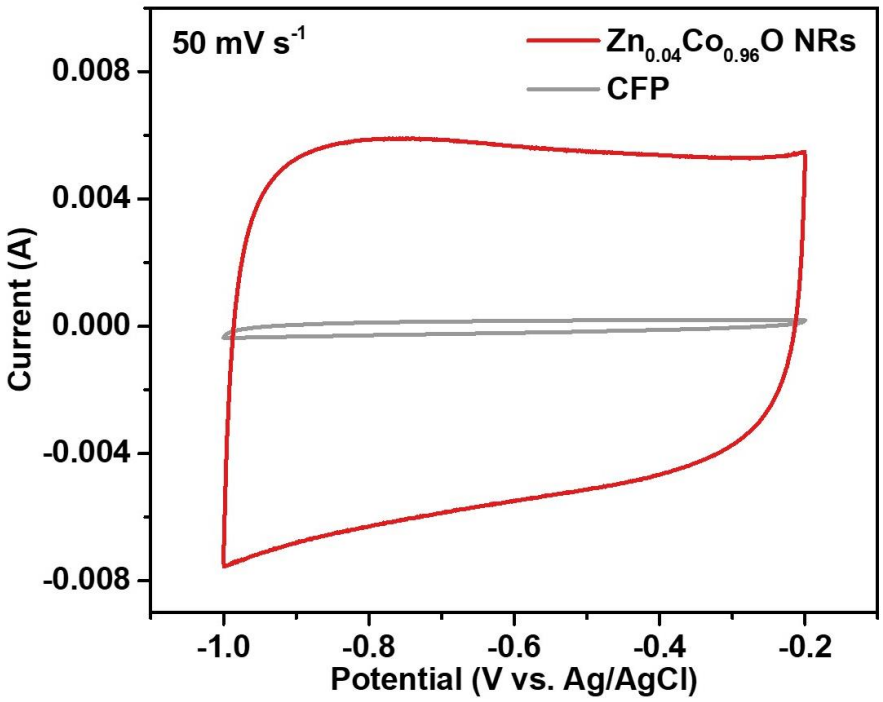

Fig. S26. CV curve of carbon fiber paper.

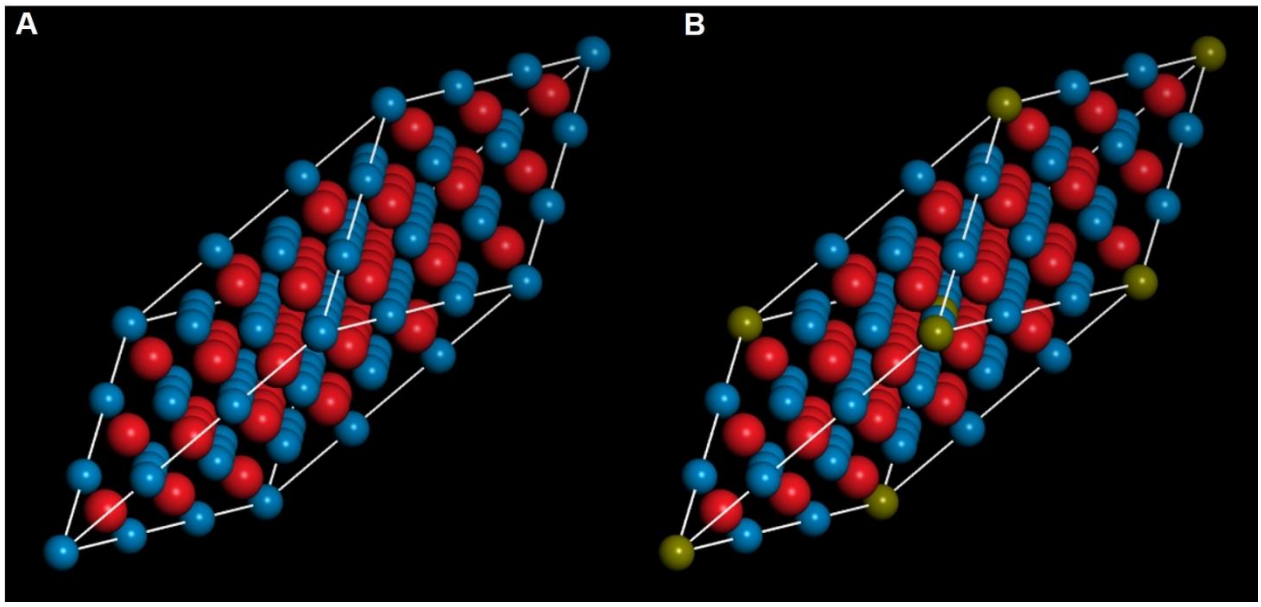

Fig. S27. Simulation models of bulk (A) CoO and (B) Zn-doped CoO. In **B**, the Zn dopant concentration is 3.7%. Colour codes: blue and red spheres denote respectively cobalt and oxygen atoms, and bluish yellow spheres denote Zn atoms.

Supplementary Tables

Table S1. Average O vacancy concentrations of $Zn_xCo_{1-x}O$ NRs measured by ICP-MS measurements.

Sample	Exchange temperature (^oC)	Bulk O-vacancy concentration, δ_{bulk}
CoO NRs	625	0.05
$Zn_{0.04}Co_{0.96}O$ NRs	600	0.034
$Zn_{0.06}Co_{0.94}O$ NRs	575	0.022

Table S2. Elemental analysis of $Zn_{0.04}Co_{0.96}O$ NRs before and after the cycling test using ICP-MS measurements.

Sample	Mass of Co^{2+} (mg cm^{-2})	Mass of Zn^{2+} (mg cm^{-2})	Total mass (mg cm^{-2})
As-prepared $Zn_{0.04}Co_{0.96}O$ NRs	0.246	0.0105	0.326
$Zn_{0.04}Co_{0.96}O$ NRs After cycling test	0.242	0.0097	0.320

Table S3. Comparative summary of the performance of $Zn_xCo_{1-x}O$ NRs in symmetric supercapacitor with the present symmetric supercapacitor and asymmetric supercapacitors.

Capacitive materials	Potential window (V)	Capacitance (F g^{-1})	Device configuration	Energy density (Wh kg^{-1})	Power density (kW kg^{-1})	Reference
$Zn_xCo_{1-x}O$	1.5	450 @ 1 V s^{-1}	SC-$Zn_xCo_{1-x}O$	67.3	1.67	This work
$LaMnO_3$	2	400 @ 0.1 V s^{-1}	SC-$LaMnO_3$	40.9	0.36	*Nat. Mater*. 2014, 13, 726
HGF[a]	3.5	310 @ 1 A g^{-1}	SC-HGF	34.6	0.28	*Nat. Commun.* 2014, 5, 4554
TiS_2/CNT[b]	3	120 @ 0.01 V s^{-1}	SC-TiS_2/CNT	60.9	0.07	*Adv. Mater.* 2018, 30, 1704754
OMFLC-N[c]	1.2	855 @ 1 A g^{-1}	SC-OMFLC-N	41.0	26.0	*Science*, 2015, 350, 1508
NPG[d]/MnO_2	0.8	1145 @ 0.05 V s^{-1}	SC-NPG/MnO_2	57	16	*Nat. Nanotech.* 2011, 6, 232
Ni-Co oxide	0.45	1900 @ 2 A g^{-1}	ASC-Ni-Co//G/MMCS[e]	52.6	1.60	*Adv. Mater*. 2017, 29, 1605902
Amorphous $Ni(OH)_2$	0.5	2188 @ 0.001 V s^{-1}	ASC-$Ni(OH)_2$// Activated carbon	35.7	0.49	*Nat. Commun.* 2013, 4, 1894
Fe_2O_3	1.0	290 @ 3.2 V s^{-1}	ASC-Fe_2O_3//MnO_2	75	3.125	*Adv. Mater.* 2018, 30, 1706640
Lithiated Graphite	1.8	-	ASC-graphite// Activated carbon	68.7	0.017	*Nat. Mater.* 2017, 17, 167
FeOOH	1.2	1066 @ 1 A g^{-1}	ASC-$NiMoO_4$//FeOOH	104	1.27	*Nat. Commun.* 2017, 8, 14264
$Ti_3C_2T_x$	0.9	200 @ 2 V s^{-1}	-	-	-	*Nature*, 2018, 557, 409
$Ti_3C_2T_x$	1.1	420 @ 0.1 V s^{-1}	-	-	-	*Nat. Energy* 2017, 2, 17105

[a]Holey graphene frameworks. [b]Carbon nanotubes. [c]N-doped ordered mesoporous few-layer carbon.

[d]Nanoporous gold. [e]Graphene/multishelled mesoporous carbon spheres.

Supplementary Notes

Note S1. Analysis of the distribution of O vacancy on $Zn_xCo_{1-x}O$ NRs.

As indicated by the EELS characterization (Figs. 2D and 2E), O-vacancies are dominantly present in the region of 2~3 nm from the outermost surface of $Zn_xCo_{1-x}O$ NRs. Using the peak shift (~0.45 eV) of the two spectra collected for site 1 and site 2 (Fig. 2E), the average O-vacancy concentration on the surface of $Zn_xCo_{1-x}O$ NR is estimated as ~22.5%. To validate further this conclusion, the average concentration of O-vacancies (δ_{bulk}) in bulk $Zn_xCo_{1-x}O$ NRs was determined by ICP-MS measurement (table S1), which gives the average information about the whole $Zn_xCo_{1-x}O$ NRs. The relation between the concentrations measured by EELS ($\delta_{surface}$) and ICP-MS (δ_{bulk}) can be correlated using the following equation

$$\frac{\delta_{surface}}{\delta_{bulk}} = \frac{V_{bulk}}{V_{surface}} \Rightarrow \frac{\delta_{surface}}{\delta_{bulk}} = \frac{\pi R^2 \cdot h}{\pi(R^2 - (R - 3\text{ nm})^2) \cdot h} \quad (6)$$

where $V_{surface}$ and V_{bulk} are the surface-region (about 3 nm from the outermost surface of CoO NRs, shown in fig. S8) and whole volume of $Zn_xCo_{1-x}O$ NRs, R and h is the radius and height of the $Zn_xCo_{1-x}O$ NRs, respectively. The average radius (R) of $Zn_xCo_{1-x}O$ NRs is estimated as 40 nm (Fig. 2A and fig. S4). For $Zn_{0.04}Co_{0.96}O$ NRs, the value of δ_{bulk} is 0.034. Hence, based on the above equation, $\delta_{surface}$ is calculated as 23.5%, which is close to what was observed by EELS (22.5%). Therefore, the O-vacancies on $Zn_xCo_{1-x}O$ NRs are indeed mostly distributed in the surface-region with high concentration, while the interior of $Zn_xCo_{1-x}O$ NRs show negligible O-vacancies. As discussed in the main text, there is a large O-vacancy concentration gradient between the surface-region and interior of $Zn_xCo_{1-x}O$ NRs. According to the Fick's second law (J. Philibert, Atomic Movements—Diffusion and Mass Transport in Solids, 1991, Les Édition de Physique), time (t) and position (x) independent diffusivity in one dimension are connected by the ordinary partial differential equation

$$\frac{\partial c(t,x)}{\partial t} = D\frac{\partial^2 c(t,x)}{\partial x^2} \quad (7)$$

where c is concentration of diffusion ions and D is the diffusion coefficient. The large O-vacancy concentration gradient , $\frac{\partial^2 c(t,x)}{\partial x^2}$, results in fast O-vacancy diffusion, $\frac{\partial c(t,x)}{\partial t}$.

Note S2. Estimation of the theoretical capacitance of P-$Zn_xCo_{1-x}O$ NRs.

It is assumed that the double layer capacitance (C_{dl}) and redox pseudocapacitance (C_{redox}) are responsible for the capacity of P-$Zn_xCo_{1-x}O$ NRs. For C_{dl}, taking into account the Brunauer-Emmet-Teller (BET) surface area of ~91 $m^2\ g^{-1}$, the surface-normalized capacitance is approximately 60 μF cm^{-2} for $Zn_xCo_{1-x}O$ film. Therefore, C_{dl} for P-$Zn_xCo_{1-x}O$ NRs should be about 55 F g^{-1}. For C_{redox}, it is assumed that low index facets, {100}, {110} and {111} are equally distributed on the surface of P-$Zn_xCo_{1-x}O$ NRs. For simplicity, we analyzed {100}, {110} and {111} of CoO. Therefore, the area per Co atom on the specific facet (fig. S13) can be calculated as

$$S_{\text{Co-}\{100\}} = \frac{a^2}{2} \tag{8}$$

$$S_{\text{Co-}\{110\}} = \frac{\sqrt{2}a^2}{2} \tag{9}$$

$$S_{\text{Co-}\{111\}} = \frac{\sqrt{3}/2a^2}{2} \tag{10}$$

where a is the lattice parameter of CoO (a=4.2612 Å). Hence, the total number of Co atoms exposed on the surface of per gram of P-$Zn_xCo_{1-x}O$ NRs can be estimated as follows

$$N = S_{\text{BET}} \times \left(\frac{1/3}{S_{\text{Co-}\{100\}}} + \frac{1/3}{S_{\text{Co-}\{110\}}} + \frac{1/6}{S_{\text{Co-}\{111\}}}\right) \tag{11}$$

where S_{BET} is the BET surface of P-$Zn_xCo_{1-x}O$ NRs. It should be noted that {111} facets of CoO are polar, which can be terminated by Co or O atoms. Therefore, the Co-terminated facets account for 1/6 fraction of the total surface area of P-$Zn_xCo_{1-x}O$ NRs. Assuming the Co oxidation state

change of surface Co atom is 2, the theoretical redox capacitance of P-$Zn_xCo_{1-x}O$ NRs was estimated by using the following equation

$$C_{\text{redox}} = \frac{2\times(N/N_A)\times M_{Zn_xCo_{1-x}O}\times F}{\Delta V \times M_{Zn_xCo_{1-x}O}} \quad (12)$$

where N_A is Avogadro constant, F is Faraday's constant (96485.3383 C mol^{-1}), ΔV is the potential sweep range, and $M_{Zn_xCo_{1-x}O}$ is the molar mass of $Zn_xCo_{1-x}O$.

In the potential window of -1~-0.2 $V_{Ag/AgCl}$, the redox pseudocapacitance of P-$Zn_xCo_{1-x}O$ NRs is negligible, because the two pairs of redox peaks related to Co^{2+}/Co^{3+} and Co^{3+}/Co^{4+} are located at potentials positive than -0.2 $V_{Ag/AgCl}$ (fig. S25A). Therefore, the total charge storage can be estimated as

$$C_{\text{total}} \approx C_{\text{dl}} = 55 \text{ F g}^{-1} \quad (13)$$

As shown in Fig. 3A and 3B, and fig. S12, the measured capacity for P-$Zn_xCo_{1-x}O$ NRs is ~34 F g^{-1}, is consistent with the estimated value, indicating that the double-layer capacitance dominates in the potential window studied.

In the potential window of -0.15-0.45 $V_{Ag/AgCl}$, the total capacity of P-$Zn_xCo_{1-x}O$ NRs can be estimated as

$$C_{\text{total}} = C_{\text{dl}} + C_{\text{redox}} = 462 \text{ F g}^{-1} \quad (14)$$

As shown in fig. S25B, this value is in agreement with the experimentally observed maximum capacity (345 F g^{-1}).

Note S3. Estimation of the theoretical capacitance of $Zn_xCo_{1-x}O$ NRs.

As revealed by Co-$L_{2,3}$ edge XAS analysis (fig. S19), the average Co oxidation state change for CoO NRs, $Zn_{0.04}Co_{0.96}O$ NRs, and $Zn_{0.06}Co_{0.94}O$ NRs is about 0.46, 0.74, and 0.72, respectively (i.e. by 0.46, 0.74, and 0.72 $\bar{e}$ per Co atom, respectively), in the potential window of -1 ~ -0.2 $V_{Ag/AgCl}$ (Fig. 4C). Correspondingly, the pseudocapacitance of CoO, $Zn_{0.04}Co_{0.96}O$ and $Zn_{0.06}Co_{0.94}O$ NRs can be calculated as 742, 1187, 1153 F g^{-1}, respectively, based on the equation

$$C_{\text{pseudo}} = \frac{n \times F}{\Delta V \times M_{Zn_xCo_{1-x}O}} \quad (15)$$

where n is the number of moles of charge transferred per mole of $Zn_xCo_{1-x}O$ NRs, F is Faraday's constant (96485.3383 C mol^{-1}), ΔV is the potential window, and $M_{Zn_xCo_{1-x}O}$ is the molar mass of $Zn_xCo_{1-x}O$ NRs. On the other side, considering the BET surface area of ~30 m^2 g^{-1} for $Zn_xCo_{1-x}O$ NRs, the value of C_{dl} should be about 18 F g^{-1}, representing a very small contribution to the total charge storage. Therefore, the capacitive charge storage occurs dominantly by oxidation of Co ions in the bulk $Zn_xCo_{1-x}O$ NRs, which is accomplished by intercalation of oxygen ions (Fig. 4A and fig. S18).

For $Zn_{0.04}Co_{0.96}O$ NRs, the oxidation of cobalt ions to Co^{3+} occurs at ~0 $V_{Ag/AgCl}$ (fig. S25A). The Co oxidation state change per Co atom in $Zn_{0.04}Co_{0.96}O$ NRs from -1 to -0.1 $V_{Ag/AgCl}$ should be 0.89 $\bar{e}$. If we assume the oxidation of cobalt ions during this potential range at the same rate, the Co oxidation state change per Co atom from -1 to -0.2 $V_{Ag/AgCl}$ should be 0.79 $\bar{e}$, thus the corresponding theoretical capacity for $Zn_{0.04}Co_{0.96}O$ NRs should be 1267 F g^{-1}. The experimentally obtained capacity for $Zn_{0.04}Co_{0.96}O$ NRs is approaching this theoretical limit.

Following this atomic engineering route, it is predicted that further capacity enhancement can be realized by multi-element doping and/or decreasing the crystal size of oxide. Assuming the net Co oxidation state change per Co atom in $Zn_xCo_{1-x}O$ NRs is 2 $\bar{e}$ (from +2 to +4), the potential window is 1.1 V (from -1 to 0.1 $V_{Ag/AgCl}$), the calculated capacity is 2341 F g^{-1} based on equation (15).

Note S4. Analysis of the oxygen intercalation mechanism in $Zn_xCo_{1-x}O$ NRs.

As discussed in the main text, the dominant charge storage mechanism in $Zn_xCo_{1-x}O$ NRs is oxygen intercalation instead of surface redox reactions, which is supported by the following experimental evidence. First, the surface redox reactions of CoO during charge and discharge process (*Energy Environ. Sci.*, 2011, 4, 4496-4499)

$$CoO + OH^- \rightleftharpoons CoOOH + e^- \quad (16)$$

$$CoOOH + OH^- \rightleftharpoons CoO_2 + H_2O + e^- \quad (17)$$

take place in the potential range from -0.1 ~ 0.4 $V_{Ag/AgCl}$ (fig. S25A), which is more positive than the potential window studied for $Zn_xCo_{1-x}O$ NRs in Fig. 3A (-1~-0.2 $V_{Ag/AgCl}$). Moreover, the main cobalt oxidation state of $Zn_xCo_{1-x}O$ NRs after cycling test remained at about 2 (fig. S15A). Second, the insertion of oxygen ions into $Zn_xCo_{1-x}O$ NRs is observed based on the O-K edge spectra of $Zn_xCo_{1-x}O$ NRs (Fig. 4A and fig. S18). Notably, the peak A originates from transition of electrons to hole states of Co3d-O2p octahedral coordination (*Chem. Mater.* 2010, 22, 70-76). Due to the presence of a large amount of O-vacancies, peak A for the as-prepared $Zn_xCo_{1-x}O$ NRs is not obvious, however, it rises up significantly after processing at -0.2 $V_{Ag/AgCl}$, indicating the increased oxygen content in $Zn_xCo_{1-x}O$ NRs. Third, the average Co oxidation state change for $Zn_{0.04}Co_{0.96}O$ NRs is 0.74 $\bar{e}$ per Co atom. This demonstrates that the oxygen ions are intercalated into the inner part of $Zn_xCo_{1-x}O$ NRs because their surface area is relatively low (~30 $m^2 g^{-1}$). Last, the small difference in the Co oxidation state change between $Zn_{0.04}Co_{0.96}O$ and $Zn_{0.06}Co_{0.94}O$ NRs accords well with the tiny difference in the O-vacancy concentrations (table S1). Therefore, the capacitive charge storage in $Zn_xCo_{1-x}O$ NRs occurs dominantly through a mechanism of oxygen intercalation rather than surface redox reactions.

Supplementary Methods

Materials Characterizations. XRD characterization was carried out using a Bruker D8 advance XRD. XPS analysis was performed using a Kratos Axis Ultra DLD with a monochromatic Al (Kα) radiation source. M-S plots were performed on a Versastat 3 potentiostat electrochemistry workstation with a frequency of 1000 Hz.

Electrochemical performance calculations. Gravimetric-specific capacitance (C_m) of electrode materials was calculated from the CV curves by integrating the cathodic sweep using the following equation

$$C_m = \frac{1}{mv|V_a - V_b|}\int_{V_b}^{V^a} i(V)dV \tag{18}$$

where m is the mass loading of the electroactive material on the electrode, v is the scan rate, V_a and V_b are the cathodic and anodic potential, respectively, and i(V) is the current response at a specific potential V.

Energy density (E) was calculated using the following equation

$$E = \frac{1}{2}CV^2 \tag{19}$$

where C is the capacitance of the material and V is the potential window of the cell.

Power density (P) was calculated using the following equation

$$P = \frac{E}{t} \tag{20}$$

where t is the discharge time.

Computational methods. Density functional theory plus U (DFT+U) calculations were carried out using projector augmented wave (PAW) (*Phys. Rev. B* 1999, 59, 1758-1775; *Phys. Rev. B* 1994, 50, 17953-17979) pseudopotential and the Perdew-Burke-Ernzerhof (PBE) exchange-correlation functional (*Phys. Rev. Lett.* 1996, 77, 3865-3868), as implemented in the Vienna Ab-initio Simulation Package (VASP) (*Phys. Rev. B* 1993, 47, 558-561; *Comput. Mater. Sci.* 1996, 6,

15-50). For a better description of the Co 3*d* electrons, an effective U parameter of 3.7 eV under the approximation introduced by Dudarev *et al.* (*Phys. Rev. B* 1998, 57, 1505-1509) was applied.

All calculations were carried out using a plane wave kinetic energy cut-off of 400 eV. All structures in the calculations were spin-polarized and relaxed until the convergence tolerance of force on each atom was smaller than 0.05 eV. The energy converge criteria was set to be 10^{-5} eV for self-consistent calculations with a gamma-centre 2x2x1 *k*-mesh. The computational unit cells to investigate O-vacancy diffusion barriers through different surfaces are shown in fig. S20. For both {111} and strained {111} structures, one H layer was introduced to make the slab to obey the electron counting rule, which is a common method used for polar surfaces (*J. Phys.: Condens. Matter*. 2014, 26, 315014; *J. Chem. Phys.* 2013, 139, 124704). The energy barrier was located via searching for transition states by climbing image nudged-elastic band (CI-NEB) method (*J. Chem. Phys.* 2000, 113, 9901-9904) implemented in VASP. The transition states were obtained by relaxing the force below 0.05 eV $Å^{-1}$. Note that the located transition states were further confirmed by frequency analysis.